

Hard–Soft Carbon Composite Anodes with Synergistic Sodium Storage Performance

Fei Xie, Zhen Xu, Anders C. S. Jensen, Heather Au, Yaxiang Lu, Vicente Araullo-Peters, Alan J. Drew, Yong-Sheng Hu, and Maria-Magdalena Titirici*

A series of hard–soft carbon composite materials is produced from biomass and oil waste and applied as low-cost anodes for sodium-ion batteries to study the fundamentals behind the dependence of Na storage on their structural features. A good reversible capacity of 282 mAh g^{−1} is obtained at a current density of 30 mA g^{−1} with a high initial Coulombic efficiency of 80% at a carbonization temperature of only 1000 °C by adjusting the ratio of hard to soft carbon. The performance is superior to the pure hard or soft carbon anodes produced at the same temperatures. This synergy between hard and soft carbon resulting in an excellent performance is due to the blockage of some open pores in hard carbon by the soft carbon, which suppresses the solid electrolyte interface formation and increases the reversible sodium storage capacity.

from both fundamental research and industry due to the global availability of Na and its lower cost. Nonetheless, in order to compete with lithium-ion batteries (LIBs), finding low cost and high-performance electrodes for SIBs is of crucial importance. Good progress has been made in the development of suitable cathode materials based on existing research in Li-ion electrodes while trying to avoid elements like Co not to compete with Li-ion technologies.^[1–7] However, the progress in discovering suitable anodes has been significantly slower, since Na⁺ ions do not intercalate into standard graphite anodes for LIBs (unless solvated^[8]).

1. Introduction

Sodium-ion battery (SIB) technologies offer great perspectives for low-cost grid-scale energy storage systems as well as short distance transportation. They have attracted growing attention

Disordered carbon anodes are the most promising candidates for SIBs among other choices such as titanium-based materials, chalcogen-based materials, alloys and organic materials, owing to advantages such as performance, cost, sustainability, and structural stability.^[9] There are several carbonaceous materials which so far have shown good performance as anodes in SIBs such as hard carbons,^[10–12] soft carbons,^[13,14] carbon hybrids,^[15,16] expanded graphene,^[17] and heteroatom-doped carbons,^[18,19] etc.

As recently discussed by Hu and coworkers, despite their low cost, pure hard carbon precursors such as cellulose, lignin, phenolic resin, etc., can still be more expensive than some soft carbon precursors (i.e., pitch and anthracite).^[14] In addition, pure hard carbons usually show very low initial Coulombic efficiency (ICE) due to their high specific surface area when carbonized at low temperatures (below 1000 °C). Therefore, hard carbon anodes are normally treated at temperatures above 1300 °C, which adds extra costs, in addition to that from the precursor.^[10,14–16,20] Soft carbon precursors such as mesophase pitch (MP), which is a waste residue from the oil industry, are less expensive. The resulting soft carbons have more ordered structures with fewer defects and shorter interlayer spacing^[21] and, as a result, exhibit lower capacities than hard carbons.^[22]

Given the complimentary properties of hard and soft carbons, the combination of the two provides a good strategy to develop carbonaceous anode materials for SIBs with both low cost and high performance. Hu and coworkers have reported hard–soft carbon composite materials derived from phenolic resin, lignin, and pitch for SIBs with good performance.^[15,16] Their findings showed that the hard–soft carbon composite electrodes had the same capacity loss compared to solely hard


F. Xie, Dr. A. C. S. Jensen, Prof. A. J. Drew
School of Physics and Astronomy
Queen Mary University of London
London E1 4NS, UK

F. Xie, Z. Xu, Dr. H. Au, Dr. V. Araullo-Peters, Prof. M.-M. Titirici
School of Engineering and Materials Science
Queen Mary University of London
London E1 4NS, UK
E-mail: m.titirici@imperial.ac.uk, m.m.titirici@qmul.ac.uk

Dr. H. Au, Prof. M.-M. Titirici
Department of Chemical Engineering
Imperial College London
London SW7 2AZ, UK

Dr. Y. Lu, Prof. Y.-S. Hu
Key Laboratory for Renewable Energy
Beijing Key Laboratory for New Energy Materials and Devices
Institute of Physics
Chinese Academy of Sciences
School of Physical Sciences
University of Chinese Academy of Sciences
Beijing 100191, China

Prof. A. J. Drew, Prof. M.-M. Titirici
Materials Research Institute
Queen Mary University of London
London E1 4NS, UK

 The ORCID identification number(s) for the author(s) of this article can be found under <https://doi.org/10.1002/adfm.201901072>.

DOI: 10.1002/adfm.201901072

carbons carbonized at the same temperatures, and that the best performance of their electrodes could be achieved at 1400 °C.

In this work, we show that we can combine the benefits of hard and soft carbon precursors and produce a composite with a high capacity and a high ICE at a low carbonization temperature of 1000 °C compared to pure hard or soft carbon treated at the same temperature. This synergy is achieved by decreasing the surface area and Na⁺ ions consumption during solid electrolyte interface (SEI) formation, while maintaining a large number of sodium storage sites. By preparing, testing, and characterizing materials with different ratios of hard to soft carbon at different carbonization temperatures, we could tune the porosity and structural features and hence also elaborate on the Na storage mechanism to confirm that Na ions are first adsorbed at the defect sites in the sloping region while nanovoids filling happens mainly in the plateau region.

2. Results and Discussion

Hard–soft carbon composites were produced by carbonization of filter paper (FP), as a cellulose hard carbon precursor, and MP, as the soft carbon precursor. Different ratio of the two carbon precursors and varying carbonization temperatures were compared. The pure FP and MP carbonized at 1000 °C are denoted as “FP 1000” and “MP 1000”, while the resulting hard–soft carbon composites are denoted as “FP-MP a:b T” (a:b is the weight ratio of FP to MP, and T is the carbonization temperature).

The scanning electron microscopy (SEM) images in **Figure 1** show the morphologies of all the carbon samples. FP 1000

shows a fiber-like morphology while MP 1000 is more chunk-like (Figure 1a, b). When FP was mixed with a lower amount of MP (FP:MP = 5:2 by weight), the morphology of the resulting carbons maintained the fibrous features. This fiber-like appearance could also be maintained under different carbonization temperatures from 1000 °C to 1500 °C (Figure 1c,f,g). However, when the amount of MP was increased, the morphology changed to small chunks showing curved edges (Figure 1d,e) which are more similar to pure MP-derived carbon.

The microstructure of these carbon samples was also observed by transmission electron microscopy (TEM) and the images are shown in **Figure 2**. They could qualitatively show that the disordered structures observed in FP 1000 are in contrast with those of the more long-range ordered domains in MP 1000. It is obvious that with an increasing amount of MP, more long-range ordered structures could be seen. This trend also exists when the carbonization temperature is increased, indicating that the addition of MP and an increased heat treatment temperature would lead to more long-range ordered nanodomains with a higher content of graphitic structures. The selected area electron diffraction (SAED) patterns show dispersed diffraction rings and no diffraction spots for all the carbon samples, indicating the generally amorphous and turbostratic structures. The sharper diffraction rings would suggest more ordered structures with increased addition amount of MP and increased pyrolysis temperatures.

To further elucidate the microstructure of the carbon materials, X-ray diffraction (XRD), and Raman spectroscopy were employed (**Figure 3**). Two peaks centered at $2\theta \approx 24^\circ$ and 44° are

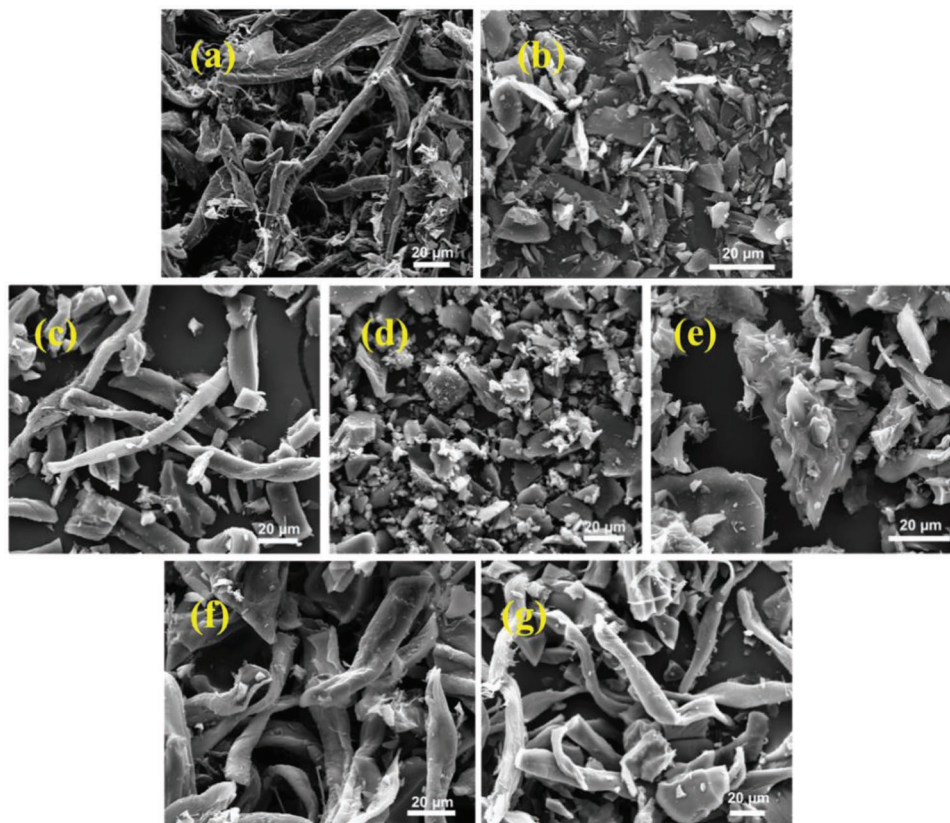


Figure 1. Morphologies of a) FP 1000, b) MP 1000, c) FP-MP 5:2 1000, d) FP-MP 1:1 1000, e) FP-MP 2:5 1000, f) FP-MP 5:2 1300, and g) FP-MP 5:2 1500.

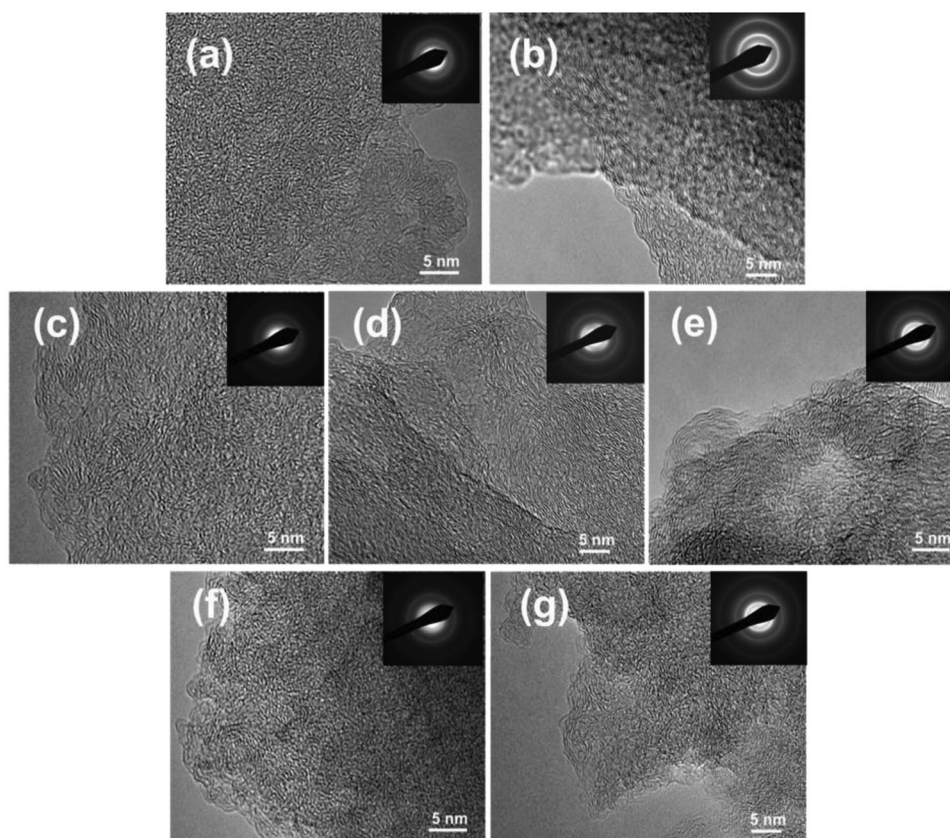


Figure 2. TEM and SAED images of a) FP 1000, b) MP 1000, c) FP-MP 5:2 1000, d) FP-MP 1:1 1000, e) FP-MP 2:5 1000, f) FP-MP 5:2 1300, and g) FP-MP 5:2 1500.

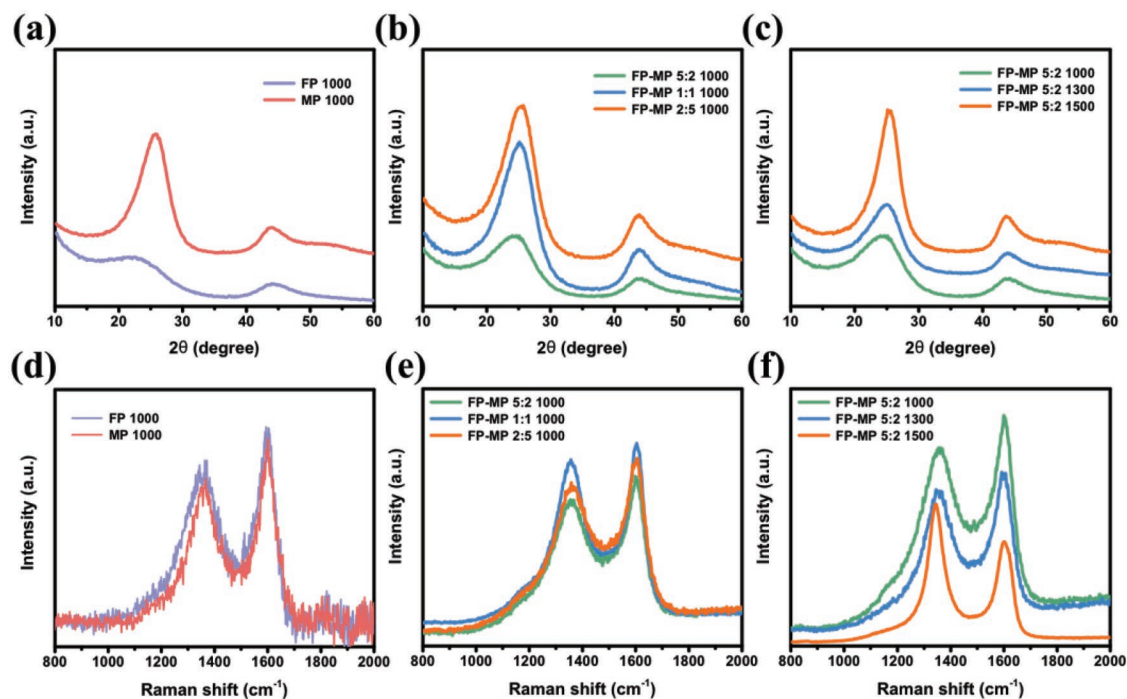


Figure 3. XRD results of a) FP 1000 and MP 1000. b) FP-MP 1000 samples with different ratios. c) FP-MP 5:2 samples at different carbonization temperatures. Raman spectra of d) FP 1000 and MP 1000. e) FP-MP 1000 samples with different ratios. f) FP-MP 5:2 samples at different carbonization temperatures.

observed for all samples (Figure 3a–c) which correspond to (002) and (100) planes of expanded graphite. FP 1000 has a very broad and weak (002) peak, suggesting poor order between graphitic planes, while the MP 1000 has a much sharper and narrower peak at a higher angle, indicating a more ordered structure and a smaller interlayer spacing. A higher fraction of MP and higher carbonization temperatures both lead to sharper and narrower (002) peaks at higher angles suggesting thicker stacks of graphitic sheets and a smaller interlayer spacing. The calculated values of d_{002} are shown in Table S1 in the Supporting Information.

Raman spectra of the carbon materials show the typical D band at around 1340 cm^{-1} and G band at around 1580 cm^{-1} (Figure 3d–f). All these carbon materials, except the FP-MP 5:2 1500, show broad signals and can be allocated in stage II of the three-stage Raman model proposed by Ferrari et al.,^[23] while the FP-MP 5:2 1500 could be in either stage I or II. This assignment was also supported by the change in full width at half maximum of the (100) peak from the XRD results (Table S2, Supporting Information). Based on this Raman model, for carbon materials in stage II, the intensity ratio of the D- to G-peaks, I_D/I_G , decrease with an increasing amount of defects in graphite layers.^[23] Therefore, since I_D/I_G decreased with an increasing ratio of MP but increased with higher pyrolysis temperatures, we conclude that increasing the ratio of MP will introduce more defects into the graphite layers, while increasing temperature results in fewer defects. The calculated in-plane size L_a based on Raman are shown in Table S1 in the Supporting Information.

According to the above characterization methods, different ratios of FP to MP and different heat treatment temperatures will definitely lead to variations in the microstructures of the resulting carbon samples. Increased temperatures result in more ordered structures and fewer curvatures or edge and surface defects as well as the in-plane defects. Increasing the amount of MP also leads to more long-range ordered nanodomains, but some defects are introduced into the graphitic layers at the same time.

N_2 adsorption and small-angle X-ray scattering (SAXS) were used to investigate the pore structure and surface area variation due to the addition of MP. Figure 4a–c shows the N_2 -adsorption isotherm of all the hard-soft carbon composite samples as well as the carbonized pure FP and MP. The pure hard carbon sample (FP 1000) shows the highest Brunauer–Emmett–Teller (BET) specific surface area of $539\text{ m}^2\text{ g}^{-1}$, typical for pure hard carbons prepared at low temperatures. When mixed with MP, the surface area of the resulting hard-soft carbon composites significantly decreases, the higher the ratio of MP to FP, the lower the surface area. The carbon derived from pure MP has the lowest surface area of only $2\text{ m}^2\text{ g}^{-1}$. Different carbonization temperatures of the FP-MP 5:2 samples did not cause significant changes in the surface area (Table S3, Supporting Information). The pore distributions of FP 1000 and FP-MP 5:2 samples are shown in Figure S1 in the Supporting Information, indicating a small number of micropores around 2 nm.

SAXS was performed to further investigate the microstructures and porosity of the resulting carbons (Figure S2,

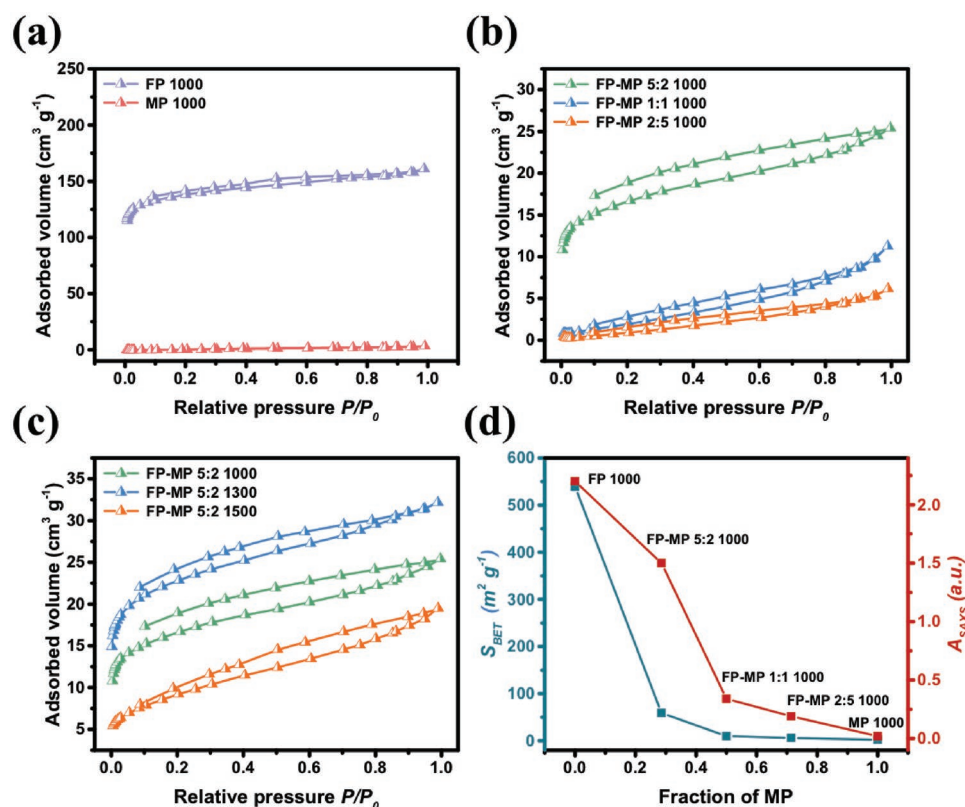


Figure 4. a–c) N_2 adsorption isotherm of all the obtained carbon samples. d) Comparison of the A parameters from SAXS in the Porod equation with BET surface area against the amount of MP.

Supporting Information). The SAXS pattern shows an initial drop and a peak around 0.3 \AA^{-1} as expected from porous carbons, indicating a mixture of large and small pores of random size and shape.^[24] The A parameter, which is proportional to the ratio of the total surface area of the large pores, shows a steady decrease from FP 1000 to MP 1000, but did not scale with the BET surface area (S_{BET}) as expected (Figure 4d, and Table S3, Supporting Information). This shows that with the addition of MP, a significant number of the pores are inaccessible to N_2 adsorption, suggesting that the soft carbon limits access to pore surface resulting in a higher fraction of closed pores. This is especially prominent in the FP-MP 5:2 1000 sample, where the trend in the A parameter and S_{BET} show the biggest difference. By comparison with the FP 1000 sample, the fraction of closed pores can be estimated to make up most of the surface area for the mixed hard-soft carbon composite sample. The nanopores were determined to be around 2 nm in size (Table S3, Supporting Information) and the surface area associated with them

decreased slightly from pure FP to the FP-MP 5:2 1000 but remained unchanged at higher fractions of soft carbon (Table S3, Supporting Information). A slight increase in the size of the nanopores was observed from 2.1 to 3 nm with increasing temperature. It is clear according to the above results that with the addition of MP, the hard-soft carbon composite materials show blocked open pores and therefore a significantly reduced BET surface area.

Electrochemical measurements were all carried at room temperatures in half cells with metallic Na as the counter electrodes. **Figure 5a** shows the discharge/charge profiles of FP 1000, MP 1000, and FP-MP 5:2 1000 in the first cycle at 30 mA g^{-1} in the potential window of 0–2.5 V. It is apparent that FP 1000 shows a huge irreversible capacity during the first cycle with a very low ICE of only 37%, resulting in a low initial charge capacity (ICC) of 150 mAh g^{-1} . MP 1000 delivers 173 mAh g^{-1} in the ICC with a high ICE of 80%. In all the composite samples the ICE and capacity significantly enhanced compared to

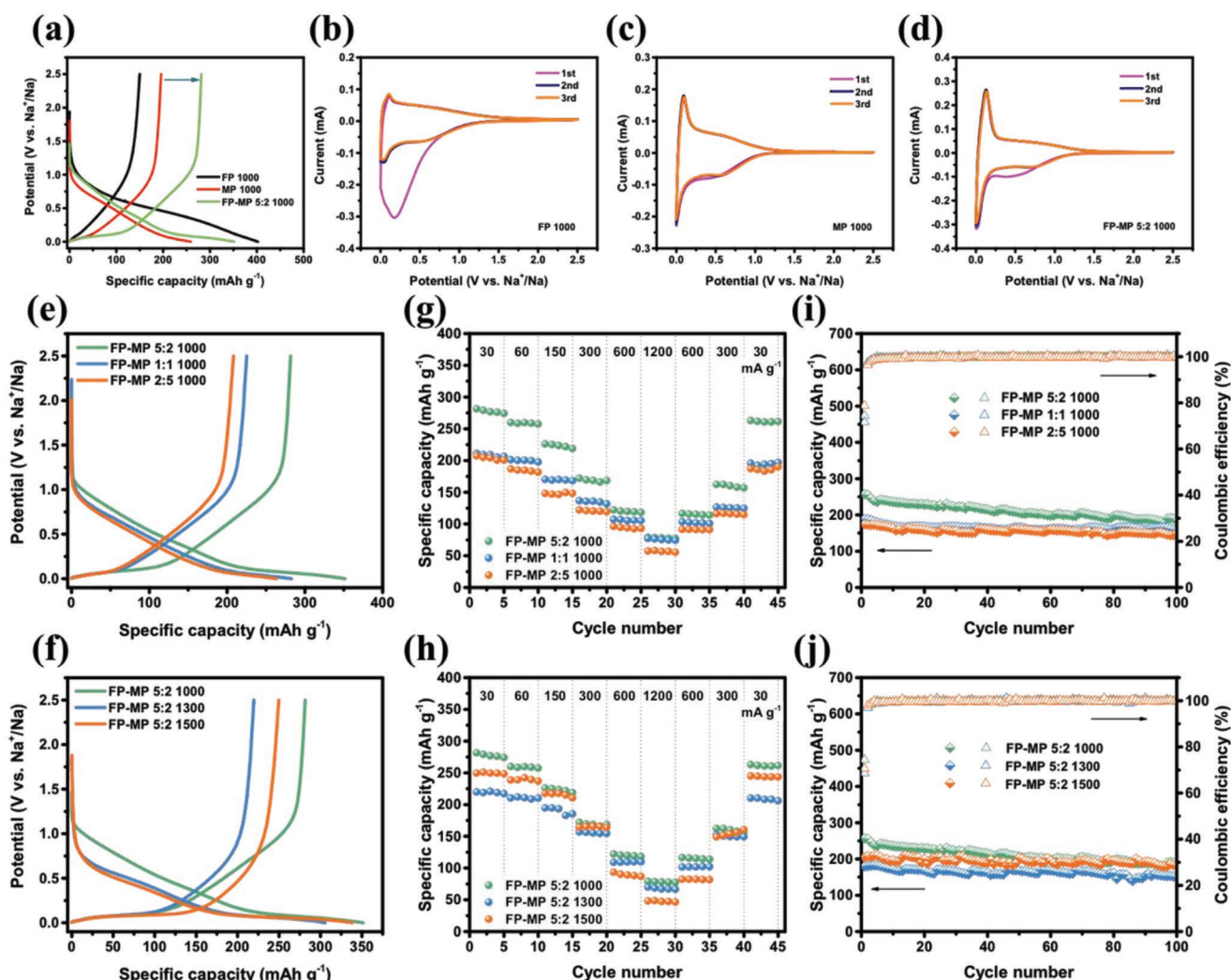


Figure 5. a) Comparison of the initial galvanostatic discharge/charge profiles of FP 1000, MP 1000, and FP-MP 5:2 1000 at 30 mA g^{-1} . b–d) CV curves of FP 1000, MP 1000, and FP-MP 5:2 1000 at 0.1 mV s^{-1} . e, f) Initial galvanostatic discharge/charge profiles of all the resulting hard-soft carbon composites at 30 mA g^{-1} . g, h) The rate capability of all the resulting hard-soft carbon composites from 30 to 1200 mA g^{-1} . i, j) The cycling performance of all the resulting hard-soft carbon composites at 150 mA g^{-1} .

FP 1000, where the FP-MP 5:2 1000 delivers a highest capacity of 282 mAh g⁻¹ with a high ICE of 80%. The discharge capacity at the first cycle also reduced from 402 mAh g⁻¹ for FP 1000 to 352 mAh g⁻¹ for FP-MP 5:2 1000. The low ICE of FP 1000 can be correlated with the high surface area and the high number of open pores, as determined by N₂ adsorption which leads to a larger electrochemistry active surface^[25] between the electrode and the electrolyte, forming a more pronounced SEI. From the combined analysis of SAXS and N₂ adsorption, it can be assumed that with the addition of MP, the pores are inaccessible to electrolyte solution, effectively protecting the electrodes from SEI formation at their surface. FP-MP 5:2 1000 shows a significantly reduced BET surface area compared with FP 1000 because of the closed pores formed which results in the increased ICE. This is corroborated by the cyclic voltammetry (CV) curves shown in Figure 5b–d, where an irreversible oxidation and reduction peaks during discharge in the first cycles corresponds to the decomposition of electrolyte and SEI formation.^[26] FP 1000 with the highest surface area has the largest irreversible peak compared to the other two samples. Higher ratio of MP and higher heat treatment temperatures only lead to minor changes of the surface area and limited variation in the ICE (Table S1, Supporting Information). In addition, the lower irreversible capacity of FP-MP 5:2 1000 compared with FP 1000 could also result from the significant reduced surface area due to the addition of MP and formation of closed pores to reduce the Na⁺ ions consumption from the SEI formation during the first cycles. The high surface area caused extra SEI formation in FP 1000 which results in fast potential changes within the electrodes during the first cycle discharge, making the voltage drop to 0 V before enough Na⁺ ions could enter and be stored within the carbon anode. With the addition of MP, the open pores are blocked, and surface area is reduced, leading to much less SEI formation, which increases the reversible capacity and cause this synergistic effect. Furthermore, the capacity will decrease with higher MP fractions (Figure 5e) because a higher amount of MP will no longer have a big contribution to block the open pores and reduce the irreversible capacity, while the more ordered structures from soft carbon would limit the total capacity. With the carbonization temperature in the FP-MP 5:2 samples increasing, the capacity first decreases to 220 mAh g⁻¹ at 1300 °C and then increases to 250 mAh g⁻¹ at 1500 °C (Figure 5f). This abnormal capacity increase at 1500 °C might result from the significantly increased *A* parameter value calculated from SAXS (Table S3, Supporting Information) for FP-MP 5:2 1500 compared with FP-MP 5:2 1000 and FP-MP 5:2 1300, suggesting that more closed pores in FP-MP 5:2 1500 were formed, which improved the sodium storage performance. The electrochemistry performance of various other reported carbonaceous materials is also compared and shown in Table S4 in the Supporting Information.

The rate capability of all carbon samples from 30 to 1200 mA g⁻¹ is shown in Figure 5g, h and Figure S3a in the Supporting Information, and the typical discharge/charge curves of the carbon samples at different current densities are shown in Figure S4 in the Supporting Information. The capacities of all the carbon samples recovered to the previous values at 30 mA g⁻¹ after cycling at higher current rates, indicating the carbon anodes are stable for a wide range of current densities. Typically,

the carbon composites with higher amount of MP and higher carbonization temperatures showed a poorer rate performance, suggesting a decreased ion diffusion at high current densities due to more ordered structures introduced from the addition of MP and increased carbonization temperatures. All the carbon composite electrodes also have better cycling performance after 100 cycles at 150 mA g⁻¹ (Figure 5i, j) compared to FP 1000 and MP 1000 (Figure S3b, Supporting Information), indicating that the combination of hard and soft carbon precursors also increases the cycling stability. It is worth noting that FP-MP 5:2 1000 retains 191 mAh g⁻¹ with 74% capacity retention, lower than the other carbon composites, which show almost no capacity fading after 100 cycles, suggesting that a higher ratio of MP and a higher pyrolysis temperature would be further beneficial for the cycling stability. The FP-MP 5:2 1000 sample was also paired with NaNi_{1/3}Fe_{1/3}Mn_{1/3}O₂ cathode for a coin type full cell. The electrochemistry properties of the full cell are shown in Figure S5 in the Supporting Information. It delivers the capacity of 252, 184, and 134 mAh g⁻¹ at 30, 600, and 1200 mA g⁻¹, respectively. And the capacity retention could be around 85% after 100 cycles at the current density of 300 mA g⁻¹.

The capacity at a high-potential sloping region above 0.12 V and low-potential plateau region below 0.12 V was calculated based on the discharge profiles in the second cycle (Table S1 and Figure S6, Supporting Information). As the amount of MP or the carbonization temperature increases, the (002) peaks in the XRD patterns become both sharper and narrower (Figure 3b,c, and Table S1, Supporting Information), indicating the presence of more ordered structures or less turbostratic nanodomains with fewer curvatures or edge and surface defects, and therefore fewer sodium storage sites. This increase in structural order may account for the decreased sloping capacity with increasing MP or carbonization temperatures (Figure 6a).^[19] The broader (002) peaks of the samples at 1000 °C with different ratios of FP to MP and higher average sloping capacity compared to the FP-MP 5:2 samples at different temperatures are also consistent with this hypothesis. The variation of *I_D/I_G* from the Raman spectra for the temperature series shows the same trend with the XRD and sloping capacity, but the trend is reversed for the MP content where more defects in the graphite layers lead to smaller sloping capacity. This might be because the capacity of sloping region depends on the defects such as curvatures, edge or surface from these turbostratic nanodomains, rather than the defects in the graphite layers.

Figure 6b shows the ex situ XRD patterns during the sodiation process from the pristine sample to 0 V. There is no obvious position shift of the (002) peaks during the sodiation process, suggesting that there seems no obvious intercalation occurring. Ex situ SAXS was also performed to study the pore filling during the sodiation process. The fits based on the modified Porod equation can be seen in Figure S7 in the Supporting Information. In the FP-MP 5:2 1000, the fitted electron density contrast $\Delta\rho$ values showed a continuous decrease followed by an increase at the end, indicating that at high sodiation level, the electron density of the pore exceeds that of the carbon matrix and vice versa at low levels, suggesting a continuous filling of the nanopores during discharging (Figure 6c, and Table S5, Supporting Information). However, we must also consider that the

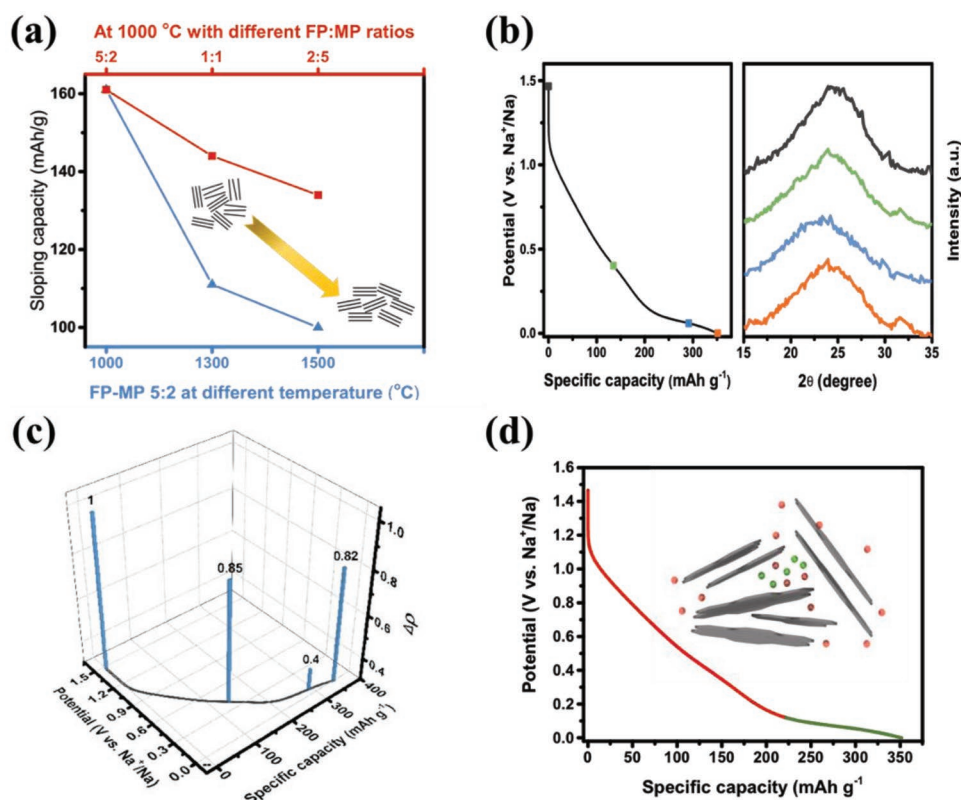


Figure 6. a) The capacity in the sloping regions decrease with both higher ratio of MP and carbonization temperatures. b) Ex situ XRD patterns during the sodiation process. c) $\Delta\rho$ values from ex situ SAXS at different sodiation states. d) Scheme of sodium storage mechanism.

SEI formation in the sloping region will also cause $\Delta\rho$ changes due to the pore filling with the electrolyte and solvated Na⁺ ions, so it may be assumed that the pore filling mechanism might mainly happens at the plateau region.

To understand the kinetic processes associated with the hard–soft carbon composites, galvanostatic intermittent titration technique (GITT) was used to determine the Na⁺ diffusion coefficients D during the sodiation process of FP-MP 5:2 1000. Figure 7a shows the typical potential profile with the discharging time with a pulse current of 30 mA g⁻¹ for 30 min and

relaxation for 2 h in the potential window 0–2.5 V. Figure 7b shows the calculated D values with the corresponding voltage during the sodiation process. It can be seen that Na⁺ ion diffusion becomes slightly slower with the decreasing voltage during the high-potential sloping region, while significantly decreasing at the plateau region, which is similar with previously reported results.^[10,27] The reason for Na⁺ ion diffusion being faster in the sloping region compared with the plateau could be attributed to different sodium storage mechanisms: defect adsorption in the sloping region is mainly a physical

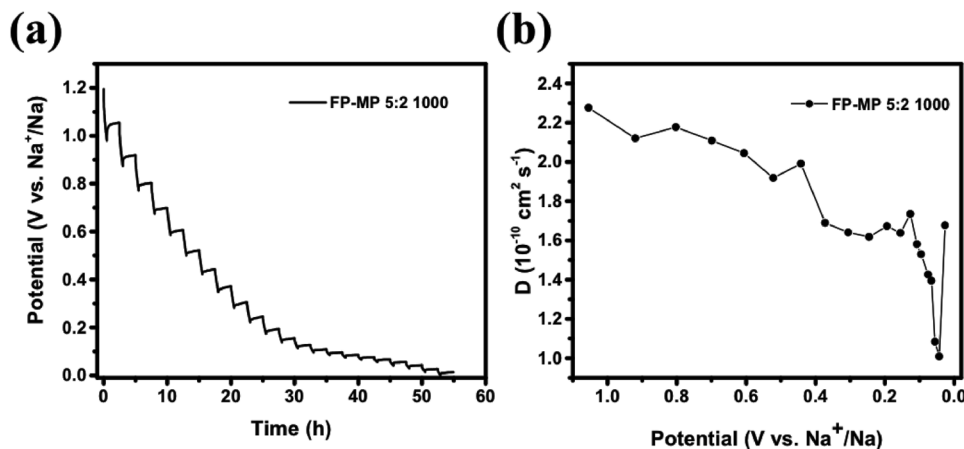


Figure 7. a) GITT potential profiles for sodiation process. b) Calculated Na⁺ ion diffusion coefficients for sodiation process.

process in which the ions diffuse faster than a redox process in the plateau region.

For the carbon materials evaluated in this work, the sodium storage mechanism could be suggested, based on our experiments, as adsorption at defects at the sloping region from the turbostratic nanodomains, and a pore filling mainly in the plateau region (Figure 6d). However, the intercalation mechanism could not be fully excluded as the (002) peaks in the XRD may be too broad to see the position changes or the intercalation is too weak to be characterized, especially for amorphous carbons treated below 2000 °C.^[28] We also believe that this kind of sodium storage model represents only one possible mechanism, which cannot be simply generalized, since all carbons differ in their microstructure and porosity. Furthermore, the ex situ measurements might have limitations on their accuracy due to artifact forming during sample preparation and require further investigation. More information about how Na⁺ gets trapped into the nanopores accounting for the plateau capacity are needed and ²³Na-nuclear magnetic resonance/magnetic resonance imaging (²³Na-NMR/MRI) are good characterization tools. Investigations are currently in progress and will be reported soon in a future manuscript.

3. Conclusions

We have synthesized a series of hard–soft carbon composite materials derived from cellulose (FP) and MP and tested them as anodes for SIBs. The combination of hard and soft carbons resulting in a composite maintains the benefits of both types of carbon and reducing the drawbacks of both, while adding a possible reduction to the electrodes cost by decreasing the carbonization temperature and the amount of hard carbon precursor. The addition of soft carbon lowers the surface area and the number of open pores, thus reducing the irreversible capacity and improving the performance in SIBs. At a relatively low carbonization temperature of 1000 °C, the hard–soft carbon composites show a synergistic effect exhibiting a better specific capacity compared with pure FP or MP. FP-MP 5:2 1000 has the highest reversible capacity of 282 mAh g^{−1} at 30 mA g^{−1} with a high ICE of 80%. This synergy is mainly because of the closed pores formed by the combination of FP and MP, which suppresses SEI formation and the associated Na⁺ ions consumption. The sodium storage mechanism elucidated by various characterization methods can be explained as Na⁺ ions adsorption at defect sites for the sloping region, while pore filling mainly occurs in the plateau region. This work also provides a basic inspiration based on tuning the microstructure/defects for the future development of low-cost carbon anode materials of SIBs by using soft carbon precursors to block open pores and enhance capacity and ICE at low carbonization temperatures.

4. Experimental Section

Materials Synthesis: MP (Bonding Chemical, USA) was dissolved in tetrahydrofuran (THF, Sigma–Aldrich, UK) using the previously reported methods.^[21,29,30] Whatman 1 FP was then soaked in different amount

of MP/THF solution to finally get the FP–MP composites with different weight ratios (FP:MP = 5:2, 1:1, and 2:5) and evaporated under mild shaking overnight. The obtained composites as well as the pure FP and MP were then carbonized at different temperatures (1000, 1300, and 1500 °C) for 1 h at 5 °C min^{−1} in N₂ atmosphere.

Materials Characterizations: The morphology of the resulting carbon materials was observed using a FEI Inspect F SEM. Quantachrome NOVA 4200 system was used to measure the N₂ adsorption–desorption isotherms. The specific surface area and pore distribution were calculated based on BET and density functional theory. The nanostructure of the samples was investigated using a JEOL 2010 TEM. A Renishaw Invia Qontor Raman spectroscopy with wavelength of 514 nm was used to investigate the Raman spectra.

Small/wide angle X-ray scattering (SAXS/WAXS) was measured on a Xenocs nano-InXider with a Cu-K_α source and a two-detector setup for combined SAXS/WAXS measurements. The samples were packed in 2 mm kapton capillaries for non-cycled samples, while sodiated samples were packed in 1.5 mm glass capillaries in an Ar-filled glove box and sealed to avoid reaction with air. The SAXS signal was analyzed using a Porod method as described by Stevens and Dahn^[24] to determine the nanovoid size and relative surface to volume ratio for the different pore sizes, this also allowed for the filling of nanovoids to be accessed. The SAXS region could be fitted well with the approach reported by Dahn's group (Figure S2, Supporting Information) as follows:^[24]

$$I(Q) = \frac{A}{Q^a} + \frac{Ba_1^4}{(1+a_1^2Q^2)^2} + C \quad (1)$$

where the A and B parameter are proportional to the ratio between the total surface area of the large and small pores, respectively. Q is the scattering vector and a is the slope of the initial drop of the intensity in the logarithmic plot (Figure S2, Supporting Information) indicating changes in the morphology of the material, where −4 would suggest a smooth interface in a multiphase system and lower values indicate a rougher interface of fractal dimensions. C is a constant background term and a₁ is characteristic length over which the scattering power changes and associated with the radius of a spherical pore volume by $R = a_1 \sqrt{10}$. The fitted values can be seen in Table S3 in the Supporting Information.

To analyze the ex situ SAXS data, the modified Porod equation was used:^[24]

$$I(Q) = \frac{A}{Q^a} + \frac{Ba_1^6\Delta\rho^2}{(1+a_1^2Q^2)^2} + \frac{C}{(1+a_2^2Q^2)^2} + D \quad (2)$$

where Δρ represents the electron density contrast, being sensitive to the changes in the electron density of pores, which is assumed to be caused by sodiation and can be set to 1 in pristine carbon.

The interlayer spacing of graphene layers d₀₀₂ was calculated based on XRD patterns by using Bragg equation.^[31] The I_D/I_G are used as the intensity ratio of D and G bands and the in-plan size L_a was calculated by using the reported equations in the literatures.^[23,32–34]

Electrochemical Measurements: CR2032 coin cells were used for all the electrochemical measurements. 95 wt.% of the carbon samples and 5 wt.% of sodium alginate as the binder were mixed with distilled water to make the slurry, which was then coated onto Al foils to make the electrodes. All the electrodes were dried in a vacuum oven at 100 °C overnight, and the active materials are kept at around 1.5–2 mg cm^{−2}. The half cells were charged and discharged within a potential window of 0–2.5 V with metallic sodium as the counter electrode. FP-MP 5:2 1000 was also paired with NaNi_{1/3}Fe_{1/3}Mn_{1/3}O₂ cathode (which is reported previously^[35]) for a full cell and tested between 1.5 and 4 V. The electrolyte is 1 M NaClO₄ in ethylene carbonate (EC) and dimethyl carbonate (DMC) (1:1, v/v) for the half cells and 1 M NaClO₄ in EC and propylene carbonate (PC) (1:1, v/v) for full cells. GF/D glass fiber was used for the separator. All the coin cells were assembled in an Ar-filled glove box. The galvanostatic charge/discharge profiles, rate and cycling performance,

and the GITT were performed on LAND CT2001A battery testing system. CV was performed on Autolab PGSTAT204 electrochemical workstation. The Na⁺ diffusion coefficients were calculated by using the equation based on Fick's second law:^[10,14,27]

$$D = \frac{4}{\pi\tau} \left(\frac{n_B V_M}{S} \right)^2 \left(\frac{\Delta E_S}{\Delta E_\tau} \right)^2 \quad (3)$$

where D is the Na⁺ diffusion coefficient, τ is the duration of pulse current, n_B and V_M are the amount of substance and molar volume of the active material, and S is the area of the electrodes. ΔE_S is the potential difference of two adjacent steady-states and ΔE_τ is the potential change due to the pulse current.

Supporting Information

Supporting Information is available from the Wiley Online Library or from the author.

Acknowledgements

The authors would like to thank Dr. Gavin Stenning for help on the Nano InXider instrument in the Materials Characterization Laboratory at the ISIS Neutron and Muon Source. M.M.T. would like to thank Engineering and Physical Sciences Research Council (EP/R021554/1 and EP/S018204/1). F.X. and Z.X. thank the China Scholarship Council for the scholarship.

Conflict of Interest

The authors declare no conflict of interest.

Keywords

closed pores, hard carbon, sodium-ion batteries, soft carbon, synergistic effect

Received: February 2, 2019

Revised: March 11, 2019

Published online: April 10, 2019

- [1] D. Yuan, W. He, F. Pei, F. Wu, Y. Wu, J. Qian, Y. Cao, X. Ai, H. Yang, *J. Mater. Chem. A* **2013**, 1, 3895.
- [2] L. Mu, S. Xu, Y. Li, Y. S. Hu, H. Li, L. Chen, X. Huang, *Adv. Mater.* **2015**, 27, 6928.
- [3] Y. You, X.-L. Wu, Y.-X. Yin, Y.-G. Guo, *Energy Environ. Sci.* **2014**, 7, 1643.
- [4] Z. Jian, W. Han, X. Lu, H. Yang, Y. S. Hu, J. Zhou, Z. Zhou, J. Li, W. Chen, D. Chen, L. Chen, *Adv. Energy Mater.* **2013**, 3, 156.
- [5] P. Barpanda, G. Oyama, S. I. Nishimura, S. C. Chung, A. Yamada, *Nat. Commun.* **2014**, 5, 1.
- [6] M. Lee, J. Hong, J. Lopez, Y. Sun, D. Feng, K. Lim, W. C. Chueh, M. F. Toney, Y. Cui, Z. Bao, *Nat. Energy* **2017**, 2, 861.
- [7] N. Yabuuchi, M. Kajiyama, J. Iwatate, H. Nishikawa, S. Hitomi, R. Okuyama, R. Usui, Y. Yamada, S. Komaba, *Nat. Mater.* **2012**, 11, 512.
- [8] B. Jache, P. Adelhelm, *Angew. Chem., Int. Ed.* **2014**, 53, 10169.
- [9] Q. Wang, C. Zhao, Y. Lu, Y. Li, Y. Zheng, Y. Qi, X. Rong, L. Jiang, X. Qi, Y. Shao, D. Pan, B. Li, Y.-S. Hu, L. Chen, *Small* **2017**, 1701835, 1701835.
- [10] Y. Li, Y. S. Hu, M. M. Titirici, L. Chen, X. Huang, *Adv. Energy Mater.* **2016**, 6, 1600659.
- [11] L. Xiao, H. Lu, Y. Fang, M. L. Sushko, Y. Cao, X. Ai, H. Yang, J. Liu, *Adv. Energy Mater.* **2018**, 1703238, 1.
- [12] P. Lu, Y. Sun, H. Xiang, X. Liang, Y. Yu, *Adv. Energy Mater.* **2018**, 8, 1.
- [13] B. Cao, H. Liu, B. Xu, Y. Lei, X. Chen, H. Song, *J. Mater. Chem. A* **2016**, 4, 6472.
- [14] Y. Li, Y. S. Hu, X. Qi, X. Rong, H. Li, X. Huang, L. Chen, *Energy Storage Mater.* **2016**, 5, 191.
- [15] Y. Li, Y.-S. Hu, H. Li, L. Chen, X. Huang, *J. Mater. Chem. A* **2016**, 4, 96.
- [16] Y. Li, L. Mu, Y. S. Hu, H. Li, L. Chen, X. Huang, *Energy Storage Mater.* **2016**, 2, 139.
- [17] Y. Wen, K. He, Y. Zhu, F. Han, Y. Xu, I. Matsuda, Y. Ishii, J. Cumings, C. Wang, *Nat. Commun.* **2014**, 5, 1.
- [18] P. Bai, Y. He, X. Zou, X. Zhao, P. Xiong, Y. Xu, *Adv. Energy Mater.* **2018**, 1703217, 1.
- [19] Z. Li, C. Bommier, Z. Sen Chong, Z. Jian, T. W. Surta, X. Wang, Z. Xing, J. C. Neuefeind, W. F. Stickle, M. Dolgos, P. A. Greaney, X. Ji, *Adv. Energy Mater.* **2017**, 7, 1.
- [20] C. Zhao, Q. Wang, Y. Lu, B. Li, L. Chen, Y. S. Hu, *Sci. Bull.* **2018**, 63, 1125.
- [21] P. Adelhelm, K. Cabrera, B. M. Smarsly, *Sci. Technol. Adv. Mater.* **2012**, 13, 015010.
- [22] W. Luo, Z. Jian, Z. Xing, W. Wang, C. Bommier, M. M. Lerner, X. Ji, *ACS Cent. Sci.* **2015**, 1, 516.
- [23] A. C. Ferrari, J. Robertson, *Phys. Rev. B* **2000**, 61, 14095.
- [24] D. A. Stevens, J. R. Dahn, *J. Electrochem. Soc.* **2000**, 147, 4428.
- [25] L. Li, Y. Xu, X. Sun, R. Chang, Y. Zhang, X. Zhang, J. Li, *Adv. Energy Mater.* **2018**, c, 1801064.
- [26] W. Luo, J. Schardt, C. Bommier, B. Wang, J. Razink, J. Simonsen, X. Ji, *J. Mater. Chem. A* **2013**, 1, 10662.
- [27] C. Bommier, T. W. Surta, M. Dolgos, X. Ji, *Nano Lett.* **2015**, 15, 5888.
- [28] B. Zhang, C. M. Ghimbeu, C. Laberty, C. Vix-Guterl, J. M. Tarascon, *Adv. Energy Mater.* **2016**, 6, 1.
- [29] Y. S. Hu, P. Adelhelm, B. M. Smarsly, S. Hore, M. Antonietti, J. Maier, *Adv. Funct. Mater.* **2007**, 17, 1873.
- [30] P. Adelhelm, Y. S. Hu, L. Chuenchom, M. Antonietti, B. M. Smarsly, J. Maier, *Adv. Mater.* **2007**, 19, 4012.
- [31] X. Ma, C. Yuan, X. Liu, *Materials (Basel)* **2014**, 7, 75.
- [32] A. C. Ferrari, J. Robertson, *Philos. Trans. R. Soc. A Math. Phys. Eng. Sci.* **2004**, 362, 2477.
- [33] A. C. Ferrari, D. M. Basko, *Nat. Nanotechnol.* **2013**, 8, 235.
- [34] M. S. Komlenok, N. R. Arutyunyan, V. V. Kononenko, E. V. Zavedeev, V. D. Frolov, A. A. Chouprik, A. S. Baturin, H. J. Scheibe, S. M. Pimenov, *Diam. Relat. Mater.* **2016**, 65, 69.
- [35] X. Yan, Y. Yang, Y.-S. He, X.-Z. Liao, H. Wang, Z.-F. Ma, *J. Electrochem. Soc.* **2016**, 163, A565.